

# Galaxy Cluster Constraints on Extensions of Modified Gravity

E. C. Diggins<sup>1</sup> and D. Wik<sup>1</sup>

University of Utah, Department of Physics and Astronomy  
e-mail: eliza.diggins@utah.edu

Received A Date, 2023; A Similar Date, 2023

## ABSTRACT

**Context.** Modified Newtonian Dynamics (MOND) has successfully matched observations on galaxy scales and made several successful, *a priori* unexpected, predictions therein; however, the paradigm fails to match observations on larger scales, specifically in groups and clusters of galaxies. To rectify these tensions, various branches of MOND theory extensions have emerged; however, many of these introduce mathematical abstractions or additional free parameters which make these extensions difficult to refute or confirm.

**Aims.** In this work, two such branches—EMOND and MOND + Dark Matter (DM)—are tested using observational and theoretical constraints which emerge from galaxy clusters. We use the theoretical framework of these extensions to predict observable deviations from the  $\Lambda$ CDM paradigm, which could serve as observational tests of these MOND extensions.

**Methods.** Fits to *CHANDRA* observations of a collection of galaxy clusters are used to constrain the asymptotic behavior of cluster temperature profiles in each MOND branch. The assumption of hydrostatic equilibrium implies very tight constraints on MOND phenomenology and introduces some non-trivial points of failure in both branches.

**Results.** We demonstrate how the MOND + DM paradigm is constrained by the imposition of hydrostatic equilibrium in galaxy clusters. We show that these constraints could be tested with upcoming X-ray missions, including XRISM. Furthermore, we illustrate significant inconsistencies in the EMOND paradigm, which suggest that extension to be non-viable in clusters of galaxies.

**Conclusions.** Modified gravity theories in the MOND research program continue to produce intriguing results on galaxy scales; however, classical theories of MOND gravity continue to fail at galaxy cluster scales. The theoretical constraints proposed in this work serve to further limit the class of viable modifications to MOND which could rectify the research program's tensions with observations of galaxy clusters. Furthermore, our findings indicate strong tensions in all of the extended paradigms considered, suggesting that further theoretical work is necessary to rectify MOND's failures on the cluster scale.

**Key words.** galaxy clusters – modified gravity – X-ray astronomy

## 1. Introduction

It is well established that gravitational systems in low acceleration regimes exhibit behaviors which are at odds with their apparent baryonic content. The appearance of this so-called missing mass is well established in many astrophysical systems, including galaxies (Rubin & Ford Jr 1970) and clusters of galaxies (Zwicky 1937). The most common resolution to the missing mass problem (MMP) is to invoke some unseen massive component in these systems which would then be able to account for the observed dynamical differences without changing the observed, and well constrained, baryonic component of the system. Many candidates for such a source of unseen mass have been proposed; however, a great many of these candidates have since been eliminated as possible sources. Hypotheses using compact objects in these systems (so-called MACHOs) have been constrained by microlensing surveys (Tisserand et al. 2007; Lasserre & Collaboration 2000) as well as by measurements of the cosmic baryon fraction, which strongly constrain the possibility for baryonic dark matter (Fukugita et al. 1998). Further explanations using more exotic forms of matter (those still well understood without altering the standard model) - particularly black holes at a variety of mass scales - have been sharply constrained by lensing surveys and would also create some inconsistencies with the cosmological predictions for the abundance of compact objects. Additionally, in the case of primordial black holes (PBHs), big bang nucleosynthesis (BBN) models place some constraints of PBH

mass ranges because PBH formation would alter the neutron-to-proton ratio (Carr et al. 2010). Nonetheless, some mass windows for black holes are still viable and actively explored as dark matter candidates (Carr & Kühnel 2020; Bertheaud et al. 2023). BBN also indicates that the baryon content of the universe,  $\Omega_b$ , must be considerably smaller than the total mass content  $\Omega_m$ , leading to the general consensus that any dark matter based theory most likely relies on some novel form of particulate mass (e.g. Ryden 2017). As with baryonic explanations for dark matter, many varieties of particle species have been proposed, of which a significant subset hold promise. Cosmological simulations by White et al. (1983) indicate that hot (relativistic) dark matter theories (HDM) would be inconsistent with galaxy-survey based observations of structure formation in the universe. This has led to the adoption of cold (non-relativistic) dark matter (CDM) as the most viable explanation for the missing mass problem, and, in doing so, forms one of the theoretical pillars of the  $\Lambda$ CDM theory of cosmology, which is widely consistent with observation.

Despite the broad success of  $\Lambda$ CDM, there remain a few inconsistencies between theoretical prediction and observation. Of greatest significance is the persistent failure to directly detect particulate dark matter (Aalseth et al. 2011a,b; Angloher et al. 2014). Furthermore, there are a litany of smaller observational inconsistencies including the tension in  $\sigma_8$  and in the Hubble constant as well as the core-cusp problem in galaxy clusters and the apparent viability of the Baryonic Tully Fisher Relation. For a recent review of tensions in  $\Lambda$ CDM, see Perivolaropou-

los & Skara (2022). Additionally, the recent launch of the James Webb Space Telescope (JWST) and its observations of galaxies at extreme redshift has introduced some degree of tension with  $\Lambda$ CDM (Labbé et al. 2023). While none of these weaknesses is capable of undermining  $\Lambda$ CDM to the point of forcing a paradigm shift, they do each represent areas of the  $\Lambda$ CDM paradigm which should be tested and challenged to better understand the underlying cause of the inconsistencies.

### 1.1. MOND

An alternative to the dark matter paradigm is to instead modify gravitational theory to resolve the MMP. The archetype of these modified gravity theories is MOND, which was originally proposed in 1983 (Milgrom 1983a,b) with the core intention of resolving the rotation curve problem observed by Rubin & Ford Jr (1970). To this end, MOND proposes 3 core axioms

1. Gravity behaves non-classically in low acceleration ( $a$ ) regimes below some fundamental  $a_0$ .
2. In the limiting case ( $a \ll a_0$ ), the acceleration is altered such that

$$\frac{a}{a_0} \mathbf{a} = \mathbf{g}_N = \mathbf{a}_N, \quad (1)$$

where  $\mathbf{g}_N$  is the equivalent, Newtonian gravitational field strength.

3. The transition from the Newtonian regime ( $a \gg a_0$ ) to the deep MOND regime, or DMR, ( $a \ll a_0$ ) occurs over a range of accelerations around  $a_0$ .

The final axiom is implemented using an *interpolation function* which connects the two asymptotic regimes and would presumably arise from a more fundamental theory.

This first theory in the MOND research program has many flaws, chief among them being its relevance only to spherically symmetric systems, and its failure to obey some of the necessary conservation laws (e.g. Felten 1984). Nonetheless, this theory made several predictions which were, *a priori*, unexpected in the  $\Lambda$ CDM paradigm. These include the Baryonic Tully-Fisher relation (BTFR), which predicts that the asymptotic speed of disk galaxies should scale with  $M^{1/4}$  (Milgrom 1983a), and the Radial Acceleration Relation (RAR), which predicts a relationship between the predicted Newtonian acceleration  $\mathbf{g}_N$  and the observed acceleration  $\mathbf{a}$  in galaxies. Both of these relations have been widely corroborated by observational studies (Lelli et al. 2016; McGaugh 2012; Verheijen 2001).

Several classical field theories have been introduced which lead to the phenomenology laid out above. The two most common are AQUAL (Bekenstein & Milgrom 1984) and QUMOND (Milgrom 2010). The AQUAL framework relies on a non-linear field lagrangian of the form

$$\mathcal{L} = \frac{\rho v^2}{2} - \rho \Phi - \frac{a_0^2}{8\pi G} \mathcal{F} \left( \frac{|\nabla \Phi|^2}{a_0^2} \right), \quad (2)$$

where  $\rho$  is the mass density,  $v$  is the velocity field,  $\Phi$  is the gravitational potential, and  $\mathcal{F}$  is an arbitrary function subject to the constraint that  $\mathcal{F}(x) \rightarrow x$  in the Newtonian regime, and  $\mathcal{F}(x) \rightarrow (2/3)x^{3/2}$  in the DMR. Variation of the Lagrangian with respect to the spatial coordinates yields the typical form of Newton's Second Law ( $\mathbf{a} = -\nabla \Phi$ ), implying that the relationship between acceleration and potential remains valid. On the other hand, variation of the Lagrangian with respect to the field itself

(see Landau 2013, for a detailed description of the approach) yields a modified Poisson equation of the form

$$\nabla \cdot \left[ \mu \left( \frac{|\nabla \Phi|}{a_0} \right) \nabla \Phi \right] = 4\pi G \rho, \quad (3)$$

where  $\mu(x) = \mathcal{F}'(x^2)$ . This  $\mu(x)$  is precisely the interpolation function described in the original theory.

Similar phenomenology is produced by the QUMOND framework with a somewhat easier mathematical formulation. QUMOND utilizes two scalar fields,  $\Psi$  and  $\Phi$ , the former being the classical, Newtonian, field and the later being the “true” field which mediates the system's behavior. The Lagrangian takes the form

$$\mathcal{L} = \frac{1}{2} \rho v^2 - \rho \Phi - \frac{1}{8\pi G} \left[ 2 \nabla \Phi \cdot \nabla \Psi - a_0^2 Q \left( \frac{|\nabla \Psi|^2}{a_0^2} \right) \right], \quad (4)$$

where  $Q$  plays a role similar to  $\mathcal{F}$  in equation 2 but instead has asymptotic behavior  $Q(z) \rightarrow z$  for  $z \gg 1$  and  $Q(z) \rightarrow (4/3)z^{3/4}$  for  $z \ll 1$ . The resulting field equations are

$$\begin{aligned} \nabla^2 \Psi &= 4\pi G \rho \\ \nabla^2 \Phi &= 4\pi G \hat{\rho} = \nabla \cdot \left( \eta \left( \frac{|\nabla \Psi|}{a_0} \right) \nabla \Psi \right), \end{aligned} \quad (5)$$

where  $\eta$  is the QUMOND interpolation function  $\eta(y) = dQ/dy^2$ . In general, QUMOND and AQUAL do not yield the same results as each Poisson equation may be written as the curl of a field, which is generally different between theories. In spherical systems, with which we are primarily interested,

$$\underbrace{\eta \left( \frac{|\nabla \Psi|}{a_0} \right) \nabla \Psi - \nabla \Phi}_{\text{QUMOND}} = \underbrace{\mu \left( \frac{|\nabla \Phi|}{a_0} \right) \nabla \Phi - \nabla \Psi}_{\text{AQUAL}}. \quad (6)$$

Thus, QUMOND and AQUAL are equivalent if and only if the two interpolation functions used are connected such that,  $\forall x \geq 0 \in \mathbb{R}, y = \eta(x)x \iff x = \mu(y)y$ . Such functions  $(\mu, \eta)$  will be referred to as *Milgromian* inverses and denoted by  $\mu = \eta^\dagger$ . In several cases throughout this work, direct knowledge of the Milgromian inverse allows for simplified computations. For a more comprehensive account of MOND's theoretical underpinnings and observational success, see Merritt (2020).

Further work on the MOND paradigm has largely focused on determining a relativistic theory which comprehensively replicates the desired MOND phenomenology while preserving the central tenants of General Relativity. Many such theories have been proposed (Bekenstein 2004; Milgrom 2009; Skordis & Zlosnik 2012); however, there has been very little progress in determining a favored theory upon which to level observational challenges. Furthermore, many relativistic MOND theories rely on different geometric and physical metrics, which typically produce a difference in the predicted speed of gravitational waves from the speed of light. Recent observations appear to be at odds with such statements (Savchenko et al. 2017). However, more recent work in relativistic MOND extensions have shown that MOND theories do exist where gravitational waves travel at the speed of light (Skordis & Złošnik 2019).

Much of this theoretical focus in the MOND paradigm focuses on establishing a relativistic theory which would provide a comprehensive foundation for MOND cosmology. While the

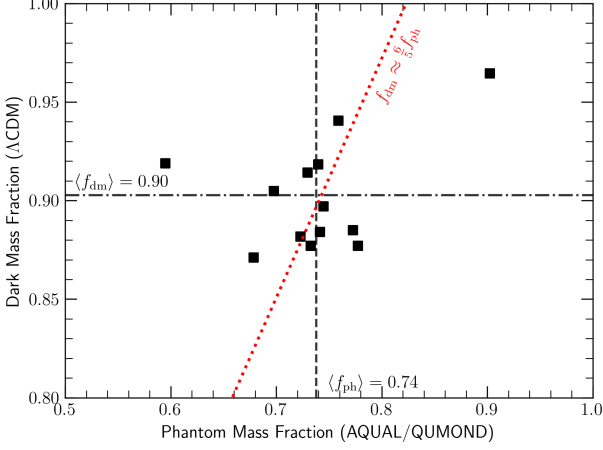


**Fig. 1.** (Presumed) dark and phantom mass fractions for each of the 13 clusters in the sample. The total internal mass of each type was measured at  $r_{\text{det}}$  corresponding to the  $3\sigma$  X-ray brightness boundary in the *Chandra* observations used to generate the models. The horizontal (vertical) line corresponds to the mean dark (phantom) mass ratio across the sample of clusters. The red line indicates the best linear fit to the scatter plot of the form  $f_{\text{dm}} = \alpha f_{\text{ph}}$ . In this sample, the missing mass problem is reduced by approximately 1/5 compared to the Newtonian case.

cosmological implications of modified gravity are certainly important, it is also crucial that such theories succeed in all non-relativistic regimes. For example, *classical* MOND (theories following the prescription of Milgrom (1983a)) remains significantly at odds with observational data in clusters of galaxies (Aguirre et al. 2001; Gerbal et al. 1992; Eckert et al. 2022).

An illustration of this is provided in Figure 1, which presents both the dark matter fraction and phantom matter fractions computed for each of the clusters in our sample. In this set of 13 clusters, MOND appears to reduce the need for “missing mass” by approximately 20%; thus persisting the necessity of some additional missing mass component, be it baryonic or otherwise. Some arguments have been made that this discrepancy results from persistent missing mass in galaxy clusters that is nonetheless still of a baryonic origin (Merritt 2020; Milgrom 2008). Others have attempted to expand the MOND paradigm (Hodson & Zhao 2017; Zhao & Famaey 2012), and still other theorists have modified the core MOND theory to account for the discrepancy, among other reasons. The most prominent of these latter approaches is the theory of superfluid dark matter proposed by Berezhiani & Khoury (2015), which has demonstrated some degree of viability in galaxy clusters (Hodson et al. 2017).

In this work, we demonstrate significant persisting tension in two popular MOND extensions: Extended MOND (EMOND) and MOND + DM. To demonstrate the significant degree of tension which still persists in each of these theories, we utilize the galaxy cluster sample from Vikhlinin et al. (2006) to explore the implications of galaxy cluster microphysics in relation to predict MOND phenomenology. The remainder of this paper is laid out as follows: in Section 2, we discuss the relevant physics in galaxy clusters for our analysis, in Section 3 we describe derivable constraints on the MOND + DM paradigm both from a theoretical perspective and through demonstrated analysis on our cluster sample. Similarly, Section 4 introduces the EMOND extension and describes its successes in galaxy clusters. We demonstrate two different approaches to the application of EMOND and discuss the constraints which can be placed on both approaches. Fi-

nally, in Section 5, we discuss the implications of our findings on the MOND paradigm as a whole and describe several interesting prospects for further observational tests of MOND extensions using upcoming observational missions.

## 2. Galaxy Clusters

Galaxy clusters form the largest dynamically stable structures in the universe, with dynamical masses on the order of  $10^{13} - 10^{15} M_{\odot}$  and physical sizes on the order of megaparsecs (Schneider 2006). In optical observations, galaxy clusters typically host on the order of 100-1000 bright galaxies within their gravitational well; however, the most significant massive components of galaxy clusters are the hot intracluster plasma (ICM) and the (apparent) dark matter halo. Typical galaxy clusters are composed of only  $\sim 5\%$  stellar mass, with an additional  $\sim 15\%$  contributed by the ICM and the remaining  $\sim 80\%$  from the presumed dark matter content (Sarazin 1986). The ICM radiates in the X-ray via thermal bremsstrahlung (Brunetti & Jones 2014), which produces an exponential emission spectrum. Spectral observations of these systems indicate temperatures on the order of  $\sim 10^8$  K, or equivalently  $kT = 1-10$  keV. Emission spectra extracted from concentric annuli can be fit to provide a projected 2D temperature profile of the cluster. A 3D model of ICM temperature may then be fit to the observed profile after projection along the line of sight and convolution with the PSF. Similarly, the gas density can be obtained from the observed surface brightness following a similar procedure. For a comprehensive account of the analysis approaches used in this process, see Eckert et al. (2022).

The end product of this analysis approach is to produce radial profiles of the gas temperature,  $T_g$ , and gas density,  $\rho_g$ , of the ICM. These analyses are typically predicated on the assumption of spherical symmetry and that the ICM plasma is in thermal equilibrium (Brunetti & Jones 2014; Vikhlinin et al. 2006; Eckert et al. 2022). While each of these assumptions introduces some degree of uncertainty, systematic studies have succeeded in producing reasonable constraints on both of these error contributions (Biffi et al. 2016; Buote & Humphrey 2012a,b).

### 2.1. Hydrostatic Equilibrium

Pressure support against gravitational collapse in the ICM may be exploited to determine dynamical masses for galaxy clusters. This is typically done by treating the ICM as a classical fluid subject to the incompressible Euler equation

$$\frac{D\mathbf{u}}{Dt} = \frac{\partial \mathbf{u}}{\partial t} + (\mathbf{u} \cdot \nabla)\mathbf{u} = -\frac{1}{\rho_g} \nabla p + \mathbf{g}, \quad (7)$$

where  $\mathbf{u}$  is the velocity field of the fluid,  $p$  is the pressure,  $\rho_g$  is the gas density, and  $\mathbf{g}$  is the gravitational acceleration. If the system is in HSE ( $D\mathbf{u}/Dt = 0$ ), then the Euler equation reduces to

$$\frac{\nabla p}{\rho_g} = \mathbf{g}. \quad (8)$$

The standard assumption in galaxy clusters is that the predominant component of the fluid’s pressure is thermal pressure from the ICM. While this approach is generally a reasonable approximation, more recent studies of hydrostatic equilibrium in galaxy clusters have indicated that non-thermal pressure support may play a non-trivial role in the dynamics of the cluster (Biffi et al. 2016; Pearce et al. 2020; Nelson et al. 2012; Lau et al. 2009). Of particular interest in the field are the influences of turbulent

pressure from bulk movements of the ICM (Pointecouteau & Silk 2005) and of the magnetic pressure present in the weakly magnetized ICM (Ensslin et al. 1997; Rosner & Tucker 1989). Because these sources of pressure are difficult to model in most cases, we assume in this work that the thermal pressure support in our cluster sample is entirely sufficient to provide for HSE. This approximation, while somewhat crude, is well constrained by simulations, which demonstrate that the ICM is typically thermal pressure dominated with non-thermal components making up only about 10% of the pressure at  $r_{200}$  (e.g. Vazza et al. 2018; Eckert et al. 2019; Nelson et al. 2014).

If thermal pressure is assumed to be dominant everywhere, we may assume an ideal gas equation of state and obtain the pressure directly from the observed temperature and density:

$$p_g = \frac{\rho_g T_g k_B}{\omega m_p}, \quad (9)$$

where  $m_p$  is the proton mass, and  $\omega$  is the mean molecular mass of the ICM, which is typically  $\sim 0.60$  (Schneider 2006). In this case, the condition for HSE may be written as

$$\nabla\Phi = -\frac{\nabla p_g}{\rho_g} = \frac{-k_B T_g}{m_p \omega} \left[ \frac{d \ln(\rho_g)}{dr} + \frac{d \ln(T_g)}{dr} \right]. \quad (10)$$

In the classical case,

$$\nabla\Phi = \frac{GM_{\text{dyn}}(< r)}{r^2} \implies M_{\text{dyn}}(< r) = \frac{r^2}{G} \nabla\Phi. \quad (11)$$

More complex models have been developed which take into account, phenomenologically, non-thermal pressure sources (e.g. Eckert et al. 2019; Shi & Komatsu 2014); however, the assumption of HSE remains the cornerstone of ICM physics and is the most precise approach used to determine the dynamical mass of systems from the gas (Eckert et al. 2022; Vikhlinin et al. 2006).

In addition to furnishing the dynamical mass of a system, hydrostatic equilibrium may also be utilized in reverse to provide the ICM temperature of a cluster given its hydrostatic parameter. This is quite useful because in cases where a MOND paradigm might alter the form of  $\nabla\Phi(\rho_g, T_g)$ , as this approach can be used to determine the resulting change in the temperature profile and therefore whether the resulting changes are consistent with the observational constraints. From Equation 10, an ODE for the temperature profile may be derived wherein

$$\frac{dT_g}{dr} + \underbrace{\frac{T_g}{\rho_g} \frac{d\rho_g}{dr}}_{T_g \Omega(r)} = \frac{-m_p \omega}{k} \nabla\Phi. \quad (12)$$

The equation has the form

$$\frac{dT_g}{dr} + T_g \Omega(r) = \Psi(r), \quad (13)$$

where  $\Omega$  is the *pressure term* and  $\Psi$  is the *acceleration term*. A complete solution of the temperature equation can be carried out by multiplying by an integrating factor of  $\rho_g$ , leading to the solution

$$T_g(r) = \frac{-m_p \omega}{k} \frac{1}{\rho_g} \int_{r_0}^r \rho_g(r') \nabla\Phi(r') dr' + \frac{\rho_g(r_0)}{\rho_g} T_g(r_0), \quad (14)$$

where  $r_0$  is a reference radius from which to begin the integration. Temperature profiles computed from equation 14 are clearly dependent on the choice of  $(r_0, T_0 = T_g(r_0))$ . When  $T_g$

is constrained by observation, all choices of  $r_0$  are self consistent and lead to the same solution curve (assuming hydrostatic equilibrium holds); however, this is not generally the case when comparing a cluster with one of different  $\nabla\Phi$ . In the context of this work, a cluster with (observationally constrained)  $T_g(r)$ ,  $\rho_g(r)$  and  $\nabla\Phi(r)$  will reproduce  $T_g$  from equation 14; however, the temperature of that same cluster with different choice of  $\nabla\Phi$  (now inconsistent with the observational  $T_g$ ) will be dependent on choice of  $(r_0, T_0)$ . The natural choice in this context is to let the choice of  $(r_0, T_0)$  be consistent with observation at some radius  $r_0$ ; however, the choice of  $r_0$  is still an arbitrary one. In this work, we adopt the convention that  $r_0 = r_{\text{max}}$ , where  $r_{\text{max}}$  is the largest radius for which the constraint on  $T_g$  is reliable.

## 2.2. The Cluster Sample

In this work, we utilize a set of 13 relaxed galaxy clusters at low redshift observed by *Chandra*. For each cluster, Vikhlinin et al. (2006) produced analytical models of cluster gas density based on matching a projected, smooth, 3D model to the observed X-ray surface brightness. A similar process was used to fit a 3D temperature model to projected temperatures found from X-ray spectra extracted from radial annuli. For a full recounting of the analysis process incorporated, see Vikhlinin et al. (2006). Density profiles were chosen to be sufficiently flexible to match the observed X-ray brightness, which is proportional to the product of the ion and electron number densities,  $n_p n_e$ . The models chosen were of the form

$$n_e n_p(r) = n_0^2 \frac{(r/r_c)^{-\alpha}}{(1 + (r/r_s)^2)^{3\beta-\alpha/2}} \frac{1}{(1 + (r/r_s)^\gamma)^{\epsilon/\gamma}} + \frac{n_0^2}{(1 + (r/r_{c2})^2)^{3\beta_2}}. \quad (15)$$

This model expands on the classic  $\beta$ -model (Cavaliere & Fusco-Femiano 1976) by allowing for a cuspy core instead of the flat core of the original model and also allowing the density to steepen at radii beyond  $0.3r_{200}$ , allowing for a successful fit to a large range of cluster phenomenologies. The gas density of the ICM is related to the emissivity measure by the relation  $\rho_g(r) \approx 1.252 m_p \sqrt{n_e n_p}$ .

Similarly, the model chosen for the ICM temperatures took the form

$$T(r) = T_0 \frac{(r/r_{\text{cool}}) + (T_{\text{min}}/T_0)}{(r/r_{\text{cool}})^{a_{\text{cool}}} - 1} \frac{(r/r_i)^{-a}}{((r/r_i)^b + 1)^{c/b}}, \quad (16)$$

which allows for a very general class of temperature profile fits. The relevant best fit parameters which were used for each of these profiles in our analysis of the cluster sample are provided in Vikhlinin et al. (2006). Wherever relevant in this work, the Planck-18 cosmology (Planck Collaboration et al. 2020) is adopted.

For each cluster, we choose values of  $r_{\text{min}}$  where cluster profiles were truncated in Vikhlinin et al. (2006) due to a variety of factors, most commonly the low fit quality in the inner regions of clusters. The authors suggest that this is due to emergent multi-phase characteristics of the ICM in the inner region, as well as observable sub-structures within the cluster centers. We follow these prescriptions for each cluster echoing Vikhlinin et al. (2006) in that our interest in these clusters is largely focused on the outer regions of the observed cluster and therefore perfect fits in the central annuli are not strictly necessary.

The presumed hydrostatic nature of the ICM provides a critical link between the gravitational phenomena being studied

and the better constrained baryonic physics observed in galaxy clusters. In the remainder of this work, the core of our analysis focuses on exploiting this link in a variety of gravitational paradigms in search of inconsistency. In any potential paradigm, the gas density  $\rho$  and the gas temperature  $T$  will clearly be invariant (they are each constrained by observation); however, the other free parameters of the system may be forced to adjust to accommodate this requirement in a new paradigm. To assure legible notation, we adopt the convention that variables consistent with a Newtonian paradigm are labeled with  $\tilde{\cdot}$  and those which are associated with the non-Newtonian paradigm are labeled without. Thus, only  $\rho$  and  $T$  are assured to have the property that  $\rho = \tilde{\rho}$  and  $T = \tilde{T}$ .

### 3. MOND + DM

One proposed modification to eliminate MOND's faults in galaxy clusters is the inclusion of an additional (collisionless) massive component which, in principle, could provide the remainder of the apparent missing mass. The exact nature of this additional component varies from theory to theory; however, popular candidates include sterile neutrinos with masses  $m_\nu \approx 11$  eV (Angus 2009; Angus et al. 2013), and cold gas content, which would not necessarily be detectable (Milgrom 2008). In either case, the inclusion of such a component is not particularly enticing; however, it remains worthwhile to test such a possibility.

Consider a galaxy cluster with some observed  $\rho_g, T_g$  and an inferred (Newtonian)  $\tilde{M}_{\text{dyn}}(< r)$ . For an alternative theory of gravity to be suitable, there must exist some possible cluster for which the same  $\rho_g$  and  $T_g$  are valid solutions. In the MOND + DM paradigm, this clearly becomes a question of whether there exists a suitable “phantom” mass distribution  $M_{\text{ph}}$  which preserves  $\rho_g$  and  $T_g$ . Assuming that  $\rho_g$  and  $T_g$  are preserved,  $\nabla\Phi$  must also be invariant between paradigms. By applying the divergence theorem to equation 3 it may be shown that,

$$M_{\text{dyn}} = \underbrace{\frac{r^2 \nabla\Phi}{G}}_{\tilde{M}_{\text{dyn}}} \mu \left( \frac{|\nabla\Phi|}{a_0} \right) = \tilde{M}_{\text{dyn}} \mu \left( \frac{|\nabla\Phi|}{a_0} \right), \quad (17)$$

where  $M_{\text{dyn}}$  is the “dynamical” or gravitational mass of the system. The resulting “phantom mass” necessary to reproduce the MOND dynamical mass is

$$M_{\text{ph}}(< r) = \underbrace{\tilde{M}_{\text{dyn}}(< r) \mu \left( \frac{|\nabla\Phi|}{a_0} \right)}_{M_{\text{dyn}}(< r)} - M_{\text{bar}}(< r), \quad (18)$$

In the DMR, ( $a \ll a_0$ ),  $\mu(x) \approx x$  and

$$M_{\text{ph}} \approx \frac{|\mathbf{a}(r)|}{a_0} \tilde{M}_{\text{dyn}}(< r) - M_{\text{bar}}(< r). \quad (19)$$

Clearly, if

$$|\mathbf{a}(r)|/a_0 \leq M_{\text{bar}}/\tilde{M}_{\text{dyn}}, \quad (20)$$

then the necessary phantom mass is negative and the solution becomes unphysical. This result provides severe constraints on the nature of any MOND + DM paradigm.

As was discussed in section 2.1, hydrostatic equilibrium is not unilaterally applicable across the entire domain of a cluster; furthermore, observations only constrain  $\rho_g$  and  $T_g$  to within

a (finite) error bound. Together, these two caveats to the idealized case presented suggest that MOND + DM type paradigms might yet escape constraint on the basis that either uncertainty in the relevant profiles or lack of true hydrostatic equilibrium could render moot any inconsistencies in our theoretical predictions. To contend with this possibility, it is worth considering at what characteristic radius of a given cluster such inconsistencies might arise.

With increasing distance from the center of mass, the ratio  $M_g/\tilde{M}_{\text{dyn}}$  should approach a constant value while  $|\mathbf{a}(r)|$  should monotonically decrease. As such, inequality 20 implies that, for any idealized model of an observed cluster, there will be some threshold radius,  $r_{\text{viable}}$ , after which the idealized system must bring on physical inconsistency. Furthermore, the inequality may be strengthened by recognizing that  $\partial_r M_{\text{phantom}} > 0$  for all radii. Thus,  $r_{\text{viable}}$  is the first radius for which this is untrue. To characterize this transition, we must consider more rigorously the best case upper bound, which we refer to as the *maximal viable radius* and denote as  $R_{\text{viable}}$ ; Appendix A provides the derivation of the below two results; for the sake of brevity, they are presented here without justification:

1. In the general case of arbitrary  $\mu(x)$ ,

$$\partial_r \tilde{M}_{\text{dyn}}(< r) \left\{ \mu(\gamma) + \gamma \partial_\gamma \mu(\gamma) \right\} - \frac{2\gamma}{r} \tilde{M}_{\text{dyn}}(< r) \mu(\gamma) \geq \partial_r M_{\text{bar}}(< r), \quad (21)$$

where  $\gamma$  is the *relative acceleration* parameter

$$\gamma = \frac{G \tilde{M}_{\text{dyn}}(< r)}{r^2 a_0}. \quad (22)$$

It should be noted that this criterion is *entirely determined by the Newtonian equivalent system*.

2. If one assumes an amenable form for  $\mu$  such that  $\mu(x) = x/(1+x^\alpha)^{1/\alpha}$ , where  $\alpha \in \mathbb{N}^+$  [a common choice in the literature (Kent 1987; Begeman et al. 1991)], then *at best*, an idealized cluster remains physical so long as

$$\frac{d \ln(\tilde{M}_{\text{dyn}})}{dr} \geq \frac{1}{r(\gamma^\alpha + 1)}. \quad (23)$$

In this special case, two phenomenologies arise dependent on  $\gamma$ .

- If  $\gamma > 1$ , then one can always select an  $\alpha$  for which the denominator on the RHS of inequality 23 is sufficiently large to satisfy the inequality at arbitrary radius and therefore cannot offer a constraint on  $r_{\text{viable}}$  without knowing (*a priori*) the value of  $\alpha$ .
- If  $\gamma \leq 1$ , then the smallest RHS for any  $r$  corresponds to  $\alpha = 1$  and therefore

$$\frac{d \ln(\tilde{M}_{\text{dyn}})}{dr} \geq \frac{1}{r(\gamma + 1)} \Leftrightarrow \rho \geq \frac{\langle \tilde{\rho}_{\text{dyn}} \rangle_r}{6}, \quad (24)$$

where  $\langle \tilde{\rho}_{\text{dyn}} \rangle_r$  is the average density over the entire cluster within a radius  $r$ .

We differentiate cluster models with best-case viability bounds dictated by  $\gamma > 1$  as having “Newtonian type viability” (NTV). Likewise, those with viability bounds dictated by  $\gamma \leq 1$  are said to possess “MONDian type viability” (MTV).

To summarize the practical implications of the results presented above, we are able to show that (assuming spherical symmetry and hydrostatic equilibrium) a galaxy cluster model is

consistent with either a Newtonian paradigm or a MOND + DM paradigm, but never both. This necessarily manifests in a critical radius,  $r_{\text{viable}}$ , beyond which *no MONDian(+DM) paradigm can replicate Newtonian phenomenology*, regardless of postulated phantom mass. Generically,  $r_{\text{viable}}$  is dependent on the distribution of baryonic mass; however, in some cases an upper bound,  $R_{\text{viable}}$ , can be placed on  $r_{\text{viable}}$  as described in the preceding paragraph. Notably, our constraints are strongest in regions where  $\gamma \ll 1$ , corresponding to the DMR.

In practice, the utility of the  $R_{\text{viable}}$  bound is a strong function of the dynamical mass profile's scale and shape. Figure 2 indicates the maximal viable radii (and corresponding minimal viable overdensities,  $\delta_{\text{viable}}$ ) over the parameter space of galaxy clusters with dynamical mass profiles following an NFW profile. We considered halos with dynamical masses between  $10^{13}$  and  $10^{15.5} M_{\odot}$  and concentration parameters between 2 and 10, corresponding to a broad range of galaxy cluster host halos. The corresponding best-fit (hydrostatic) NFW profiles to the clusters in our cluster sample are also indicated. Clearly,  $R_{\text{viable}}$  for the largest halos ( $M_{\text{vir}} > 10^{15} M_{\odot}$ ) fails to constrain the viability to within an observable radius; however, for medium-sized halos ( $10^{14} < M_{\text{vir}} < 10^{15}$ ), the usefulness of the maximal bound is dependent on the halo shape with higher concentration halos constrained within  $r_{500}$ . While X-ray observations of galaxy clusters can, on occasion, reach  $r_{200}$ , most observations are constrained to  $r < r_{500}$ . As such, clusters with viability radii within  $r_{500}$  should be ideal targets for applying the constraints discussed above. Perhaps most useful is the recognition that halos with masses below  $10^{14} M_{\odot}$  are quite frequently constrained to within  $r_{500}$ . When integrated over the parameter space, approximately 80%, 45%, and 18% of halos are constrained to within  $r_{200}$ ,  $r_{500}$ , and  $r_{1000}$  respectively.

When information is available about the cluster's baryonic mass distribution (as is the case for our cluster sample), the upper bound on  $r_{\text{viable}}$  may be replaced in favor of empirical calculation of the true viability radius. Doing so clearly relies on the assumption that the methodology by which the baryonic mass distribution was obtained is sufficiently precise, which (in practice), likely becomes the most involved part of such an analysis. Nonetheless, such an analysis was performed for our cluster sample under the assumption that the temperature and density profiles were correct within the observed region of each cluster: the radius of the inner-most annulus ( $r_{\text{min}}$ ) to *Chandra's*  $3\sigma$  detection boundary for the cluster,  $r_{3\sigma}$ . In some cases, dynamical mass profiles from Vikhlinin et al. (2006) were non-physical in the inner-most region. To counter this, we let  $r_{\text{min}}$  be either the inner-most annulus or the minimal radius at which  $M_{\text{dym}}$  (as computed from HSE) is physical, whichever is largest. When  $r_{\text{min}}$  doesn't correspond to the inner most annulus, we denote that radius as  $r_{\text{CXO,min}}$  to indicate that it is the limit of the observational domain. Figure 3 indicates these  $r_{\text{viable}}$  for each of the clusters in our sample. In two cases, no failure point was found within  $[r_{\text{min}}, r_{3\sigma}]$  (MKW 4 and RXJ 1159+5531). In all other clusters, not only was a failure point found on the basis of equation 21, but all of the viability radii found were within  $r_{500}$  for their respective cluster.

In suitable clusters, the results illustrated above suggest that the contradictory behavior of the phantom mass profile can happen well within regions of the cluster for which hydrostatic equilibrium is a reasonable assumption; however, little has yet been said about what this constraint would imply observationally. Thus far, our arguments have relied only on the hydrostatic assumption, particularly that  $\nabla\Phi = \nabla\tilde{\Phi}$ ; however, a more physically illustrative version of the same argument may be obtained

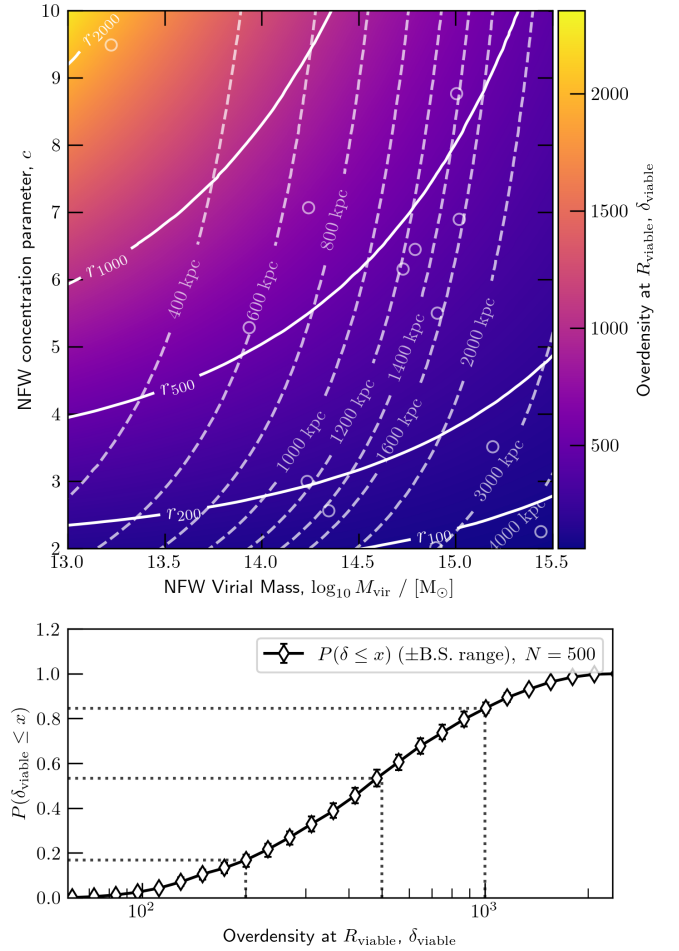


**Fig. 2.** Maximal viable radii ( $R_{\text{viable}}$ ) and corresponding overdensities,  $\delta_{\text{viable}}$ , for galaxy clusters when  $\mu(x) = 1/(1+x)$  and total mass is modeled as an NFW profile. NFW profiles were selected from the Monte-Carlo sampling ( $N = 20,000$ ) and interpolated to produce the heat map in the top panel. Each cluster in the sample procured from Vikhlinin et al. (2006) are indicated (by best-fit to NFW parameters) with circles. The bottom panel indicates the probability distribution of minimal viable overdensities (corresponding to maximal viable radii) as determined from the Monte-Carlo scheme. Error bars indicate the full interval of the bootstrapped probability in each bin when 500 iterations were performed. A Planck-18 cosmology was used and all halos were at  $z = 0.05$ .

instead by explicit examination of equation 10. If one assumes that (over some region of interest),  $\rho_g \propto r^\alpha$  and  $T_g \propto r^\beta$ , then  $\nabla\Phi \propto r^{\beta-1}$ . Furthermore, Newtonian dynamics would imply that  $M_{\text{dyn}} \propto r^{\beta+1}$ . Thus, for the dynamical mass to be stable,  $\beta = -1$  for large  $r$ . From the perspective of MOND,

$$M_{\text{dyn}} = \tilde{M}_{\text{dyn}} \mu \left( \frac{|\nabla\Phi|}{a_0} \right) \propto r^{2\beta} \quad (25)$$

for  $r$  sufficient to treat  $\mu(x) \approx x$ . For the dynamical mass to be stable in a MONDian paradigm,  $\beta = 0$  for large  $r$ . Thus, the constraints described in this section should emerge in an observational sense from the asymptotic behavior of the relevant temperature profiles. More generally, it is possible to explore the emergence of inconsistency by “correcting” MONDian systems so as to produce a self-consistent system which is minimally different from the equivalent system in the Newtonian paradigm. If the resulting deviations in the temperature profile are sufficiently large



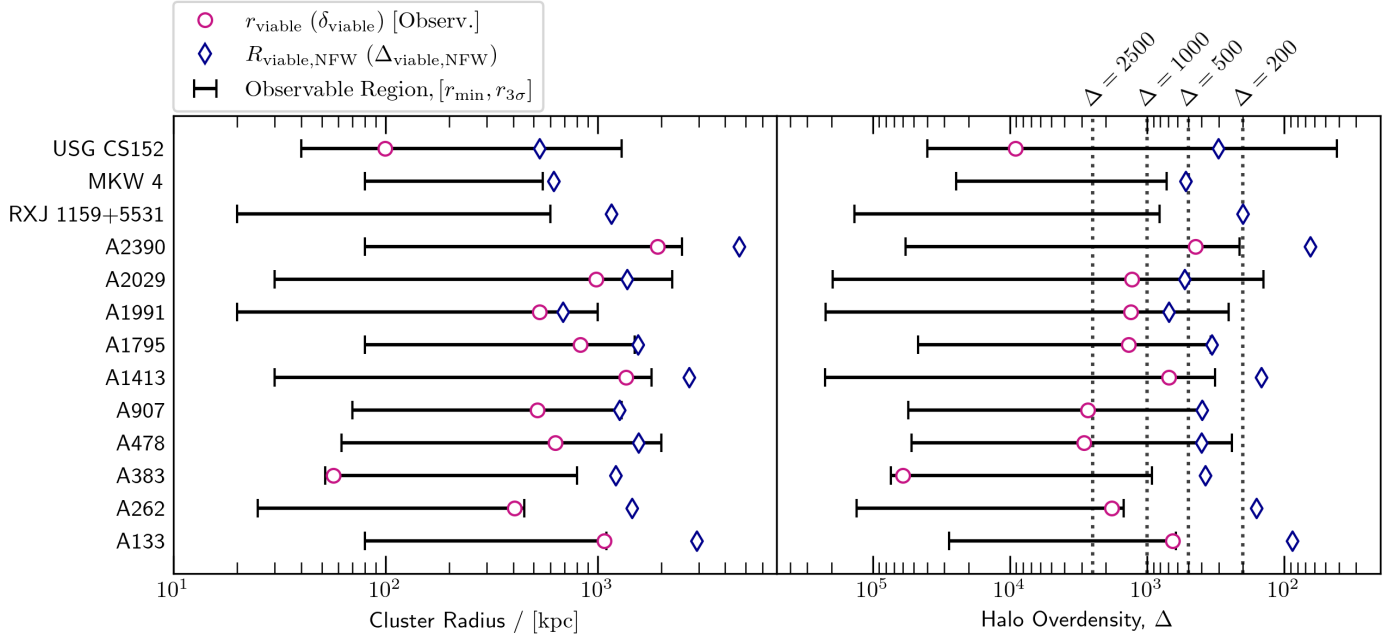


**Fig. 3.** Calculated values of  $r_{\text{viable}}$  (left panel) and  $\delta_{\text{viable}}$  (right panel) for each of the clusters in our sample. Each cluster is only physically consistent within  $r_{\text{viable}}$ . The corresponding best-fit  $R_{\text{viable,NFW}}$  and  $\Delta_{\text{viable,NFW}}$  (representing the mathematical best-case) constraints are also provided for comparison. Values of  $r$  and  $\delta$  are omitted if viability did not fail within the *Chandra* observation range. NFW best fits used a Planck-18 cosmology and the observed redshifts of each cluster (see Vikhlinin et al. 2006).

and appear at sufficiently low radii, it should be possible to comprehensively refute the MOND + DM paradigm in galaxy clusters. To that end, we conclude this section by carrying out this “correction” on the sample of cluster models described in section 2.2. Corrections are performed on the basis of equation 18; first, the implied (potentially inconsistent) dynamical and phantom mass profiles are produced using the known  $\rho_g$  and  $T_g$  profiles. To correct the emergent inconsistencies,  $\rho_{\text{dyn}} \rightarrow \rho'_{\text{dyn}}$  where  $\rho'_{\text{dyn}}$  is everywhere  $\geq \rho_g$  and therefore implies  $\rho_{\text{phantom}} \geq 0$ . There is no guarantee that such a correction produces a “smooth”  $\rho'_{\text{dyn}}$ ; however, all other correction procedures, which might be more physical, create a larger deviation in the underlying profiles. As such, we refer to this approach as “minimum” correction and conclude that other correction approach will only exacerbate our findings.

Once the corrected  $\rho'_{\text{dyn}}$  has been produced, the temperature may be recalculated directly from equation 14. Because the gravitational field will generally be changed by correction, the solution curves of the temperature equation are no longer independent of the boundary condition (as described following the introduction of equation 14). In keeping with our chosen convention, we require that the *corrected* temperature profiles be equal to the observed profiles at the outer edge of the available constraints ( $r_{3\sigma}$ ) and therefore that

$$T(r) = \frac{m_p \omega}{k \rho_g} \int_r^{r_0} \rho_g(\xi) \nabla \Phi(\xi) d\xi + T_0 \quad (26)$$

where  $T_0$  is the fixed temperature of the cluster at  $r_0$  regardless of the theoretical framework.

The computed temperature profiles are provided in Figure 4 and clearly indicate the expected divergence in the MOND + DM approach. Only clusters RXJ1159+5531 and MKW 4 are in agreement with the original temperature profile. This observation matches our prediction on the basis of the calculated  $r_{\text{viable}}$  as Figure 3 shows that those two clusters are the one ones for

which the viability radius is outside of the observable field of view. It is noteworthy that XRISM’s Extend instrument should be able to extend the relevant domain of observation, possibly increasing the number of clusters for which these deviations are observable and therefore bolster the cluster population on which one could level arguments for or against MOND + DM predicated on this analysis. Furthermore, the cluster sample presented here is by no means a comprehensive set of clusters. A wider study, in the same ilk as this one, might consider a larger set of clusters on which to perform this analysis and considerably expand the candidate clusters for which these deviations are both predicted and observable.

#### 4. EMOND

In seeking an explanation for the disparity in MOND’s utility between galaxies and clusters of galaxies, it has long been observed that, because of the size of the gravitational well in clusters, MOND phenomenology does not become dominant except in the outskirts of the system, by which point it cannot “catch up” to the necessary dynamical mass. Extended MOND (EMOND) provides an exculpatory mechanism by which to avoid this issue. Instead of mediating the transition between Newtonian and MONDian dynamics at a constant  $a_0$ , one instead uses some  $A_0(\Phi)$ . If  $A_0(\Phi)$  is some (presumably increasing) function of  $\Phi$ , then clusters would have a higher  $a_0$  cutoff than galaxies and thus a larger domain on which MOND phenomenology can occur. A classical lagrangian was introduced in Zhao & Famaey (2012, hereafter ZF12), which does just that:

$$\mathcal{L}_E = \frac{1}{2} \rho v^2 - \rho \Phi - \frac{\Lambda}{8\pi G} \mathcal{F} \left( \frac{|\nabla \Phi|^2}{\Lambda} \right), \quad \Lambda(\Phi) = A_0(\Phi)^2. \quad (27)$$

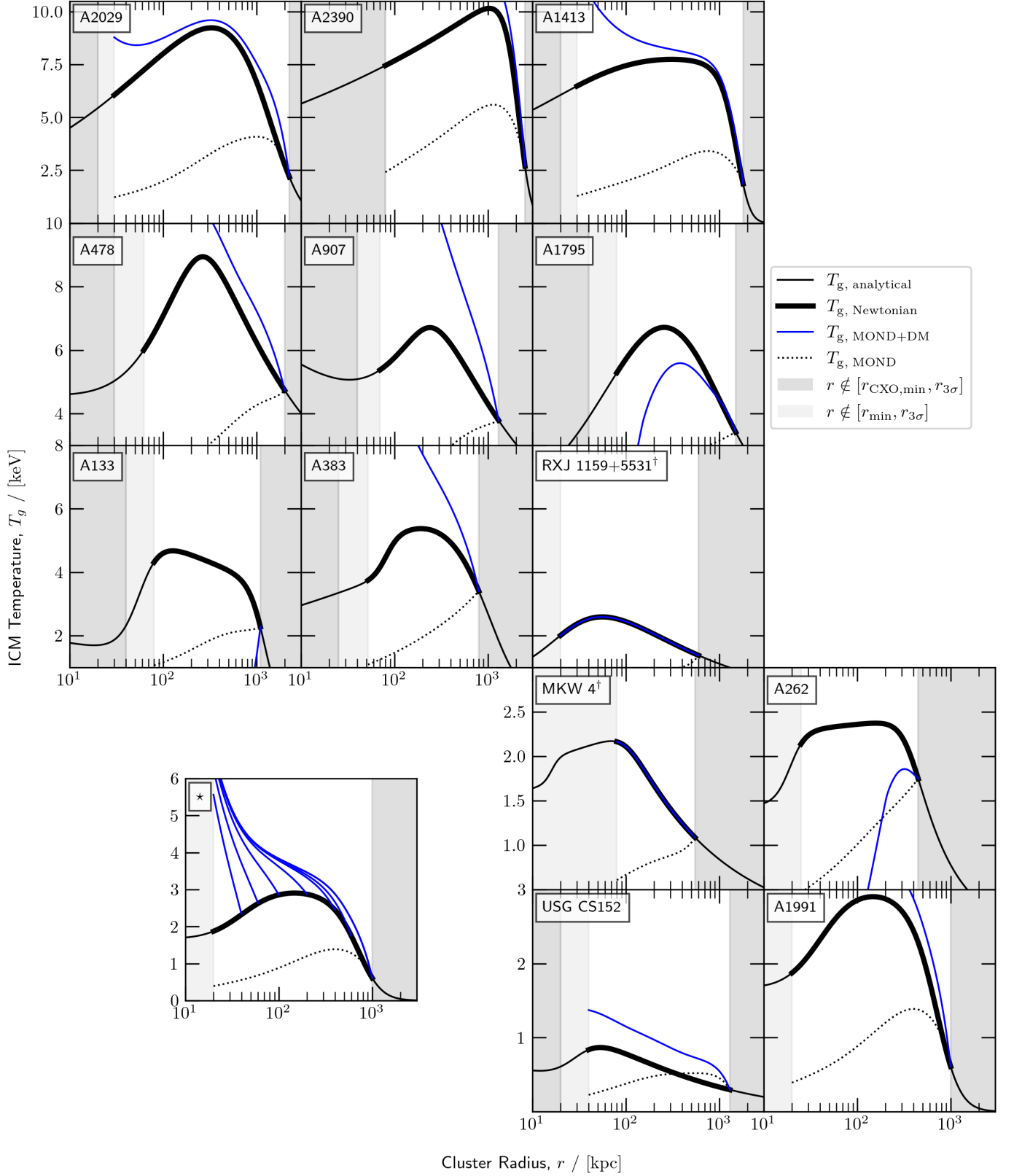


**Fig. 4.** ICM temperature curves for each cluster in our sample under different gravitational paradigms. With the exception of  $T_{g, \text{analytical}}$ , profiles were computed using equation 14 with the relevant gravitational alterations.  $T_{g, \text{analytical}}$  indicates the ICM temperature profile suggested in Vikhlinin et al. (2006) and is provided for illustration only. In all cases  $r_0 = r_{3\sigma}$  for each cluster and  $T_0 = T_{g, \text{analytical}}(r_0)$ . Shaded regions indicate radii outside of the observed domain  $[r_{\text{CXO,min}}, r_{3\sigma}]$  (dark grey) and radii outside of the physical region  $[r_{\text{min}}, r_{3\sigma}]$  (light grey). <sup>†</sup>Temperature profiles are self-consistent because  $r_{\text{viable}} \geq r_{3\sigma}$  for the indicated cluster. Panel ★ replicates the results from cluster A1991 for a variety of boundary points  $r_0$  on the temperature equation to indicate the relevance of our conventional choice.



The resulting Poisson Equation takes the form

$$4\pi G\rho = \nabla \cdot \left[ \mu \left( \frac{|\nabla\Phi|}{A_0(\Phi)} \right) \nabla\Phi \right] - \underbrace{\frac{1}{2} |\partial_\Phi \Lambda| \left( \frac{|\nabla\Phi|^2}{\Lambda} \mathcal{F}' \left( \frac{|\nabla\Phi|^2}{\Lambda} \right) - \mathcal{F} \left( \frac{|\nabla\Phi|^2}{\Lambda} \right) \right)}_{T_2}. \quad (28)$$

It is shown in ZF12 that the  $T_2$  term is typically quite small, allowing for an approximation which maintains the Gaussian characteristics of the classical Poisson equation,

$$4\pi G\rho \approx \nabla \cdot \left[ \mu \left( \frac{|\nabla\Phi|}{A_0(\Phi)} \right) \nabla\Phi \right]. \quad (29)$$

By introducing additional freedom, EMOND avoids many of the theoretical pitfalls present in more established MOND flavours; however,  $A_0(\Phi)$  cannot be left entirely unconstrained. While it is generically true that any idealized cluster model has some  $A_0(\Phi)$  which would suffice to eliminate the missing mass problem while preserving the temperature and density profiles, one expects that  $A_0(\Phi)$  should arise from some more fundamental theory and therefore that  $A_0(\Phi)$  should be uniform across different systems. Hodson & Zhao (2017, hereafter HZ17) argued that such an  $A_0(\Phi)$  was observed in the same collection of galaxy clusters described in section 2.2; however, considerable scatter was present in their findings. To explain the scatter, one must conclude that observations of the system are sufficiently uncertain to allow for such a breadth of difference. To test this assumption, we will present an extension of the work presented in HZ17 to consider the implications of the scatter in  $A_0(\Phi)$  and whether it can be described by uncertainty in the underlying profiles.

In the formalism of EMOND, the unique  $A_0(\Phi)$  curve for a given idealized cluster is given by

$$A_0(\Phi) = |\nabla\Phi| \chi \left( \frac{\nabla\Psi_b}{\nabla\Phi} \right), \quad (30)$$

where  $\chi = 1/\mu^{-1}$  and  $\Psi_b$  is the *Newtonian* gravitational potential generated by only the baryonic component of the system. Generally, equation 30 is a differential equation in  $\Phi$ ; however, by enforcing hydrostatic equilibrium,  $\Phi(r)$  may be determined to within a choice of gauge. Furthermore, if  $\Phi$  is a monotone function of  $r$  ( $\nabla\Phi > 0$  for all  $r$ ), then  $r = \Phi^{-1}(\Phi(r))$  and  $A_0(\Phi)$  may be constructed as a function of the potential without solving the ODE directly.

Because  $A_0$  is a function of the potential in EMOND, it is no longer invariant to change in the gauge  $\Phi \rightarrow \Phi + \Phi_0$ . Indeed, there is no easy resolution to this feature, even when *ad hoc* approaches are permitted in services of a (presumed) fundamental theory. Asymptotically flat boundary conditions are infeasible given that the MOND potential must go as  $\ln(r)$ ; as such, we are forced to adopt non-asymptotic boundaries. Generically, this is not an issue when computing  $A_0(\Phi)$  for a single cluster; one may simply choose a convenient gauge and proceed naturally. Any other choice of gauge simply shifts  $A_0(\Phi)$  along its domain. Issues arise when comparing the "ideal"  $A_0(\phi)$  between clusters as it then becomes necessary to choose a gauge for each cluster which is "self-consistent" between them. HZ17 adopted the convention of fitting each cluster's gravitational field to an NFW and adopting the the gauges provided by those fits. The intuition for this choice is that it implies some "universal" sense of gauge; however, the NFW profile is not a valid solution in MOND meaning that we are necessarily assuming some

heuristic connection between NFW halos and their (presumed) equivalent in MOND. Additionally, HZ17's assertion that NFW profiles fit the dynamical mass profile well is debatable; often varying by as much as half an order of magnitude in potential. More problematic is the reverse operation: given a theoretical  $A_0(\Phi)$  compute the dynamical properties of the cluster. In this case, the differential equation *requires* a choice of gauge which will necessarily impact the results and which has no physical reason to be related to the NFW profile in any way. In this work, we provide an alternate procedure for prescribing the gauge; instead of using NFW fits to the cluster models, we instead use a standardized gauge such that  $\Phi(r_{200}) = 0$ . The *Chandra* observations underlying our cluster sample are constrained (by X-ray brightness) to an outer radius  $r_{3\sigma}$  for each cluster as described previously. Because  $r_{3\sigma}$  may be less than the corresponding  $r_{200}$ , the following convention is adopted. When a cluster extends as far as  $r_{200}$ , its gravitational field is integrated in quadrature and the gauge adjusted to be zero at  $r_{200}$ . If  $r_{200}$  is outside of the model domain, the cluster is truncated at  $r_{3\sigma}$  and the gravitational field is extended (under that truncation) to  $r_{200}$  and then integrated in quadrature. The choice to enforce this boundary condition is justified by two observations; first, because the acceleration in MONDian gravity goes as  $1/r$  at large radii, the potential is logarithmic and therefore not bounded in the limit as  $r \rightarrow \infty$ . Thus, one *must* enforce a zero point of the potential at some finite radius. As for why to set that zero point at  $r_{200}$ , we argue that the potential at that radius represents (to the best extent possible) the "cosmological zero-point" which itself should naturally endow each cluster with a self-consistent choice of gauge sufficient for comparing calculated  $A_0(\Phi)$  curves. It should also be noted that, when transformed under a change of gravitational gauge  $\phi \rightarrow \Phi = \phi + \phi_0$ ,  $A_0(\phi) \rightarrow A(\Phi - \phi_0)$  with no change in shape. Thus, any observed scatter in the calculated  $A_0$  is, save for a shift in the domain, "frozen" into the data regardless of the choice of gauge. Nonetheless, the reliance of EMOND on a (necessarily *ad hoc*) choice of boundary should be considered with severe skepticism for the entire theoretical framework.

Having established a justification for the selected boundary condition, for each of the clusters in our sample, the corresponding  $A_0(\Phi)$  curve was calculated as prescribed above. To minimize the emergence of numerical artifacts, we adopt an interpolation function  $\mu(x) = x/(1+x)$  as was done in Section 3. For this choice of  $\mu$ ,  $\chi(x) = (1-x)/x$ , and  $A_0(\Phi)$  curves may be constructed as described previously. For the clusters in our sample, each had  $r_{200} < r_{3\sigma}$  and so no extrapolation was necessary. This is largely because the  $r_{200}$  is calculated, in this case, on the basis only of the baryonic component of the model, substantially reducing all of the concentration radii  $r_\Delta$ . Similar to the findings of HZ17, we do observe a clear correlation in the general shape of the necessary  $A_0(\Phi)$  curves; however, several significant differences are apparent. Of primary interest is the fact that the overall range of  $A_0(\Phi)$  values calculated in our approach is substantially larger than in HZ17, spanning approximately an order of magnitude greater set of accelerations. In an effort to determine to what degree our approach corresponds to the findings of HZ17, the theoretical form of  $A_0(\Phi) = a_0 \exp(\Phi/\Phi_0)$  (as was used in that work) was fit to our  $A_0(\Phi)$  curves.

Doing so illustrates one of the serious complications arising for the gauge choice in this framework. Because our choice of gauge does not place the zero point in a region of the cluster where  $\nabla\Phi$  is also near zero, the asymptotic behavior of  $A_0(\Phi) \rightarrow a_0$  as  $\Phi \rightarrow 0$  is not present in our approach. Given that  $A_0(\Phi)$  should arise from some more fundamental theory, the fact that change in gravitational gauge can impede upon the asymptotic

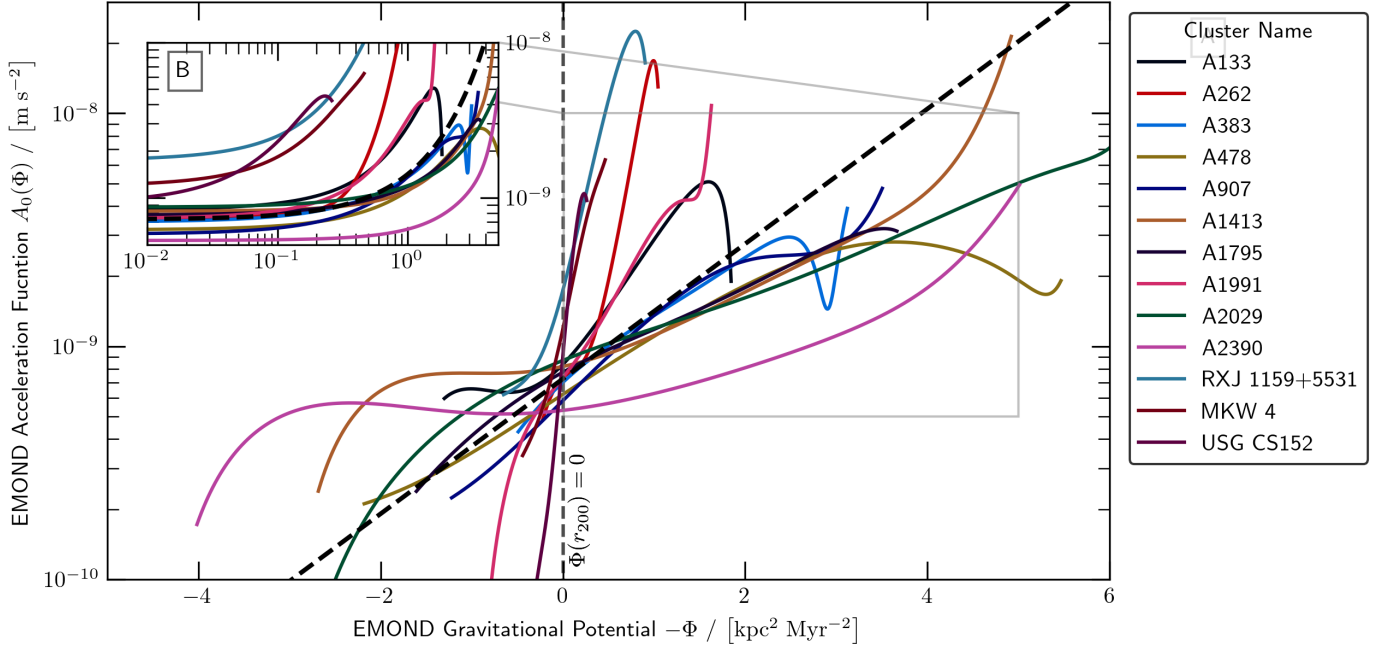


**Fig. 5.** Calculated  $A_0(\Phi)$  curves for each of the cluster models in our sample. The function  $a \exp(\Phi/\Phi_0)$  was fit using a least-squares approach to the calculated curves (black dashed). Panel A shows a symmetrically logarithmic scaling of the calculated  $A_0(\Phi)$  curves as they pass through the gauge point at  $r_{200}$ . Panel B shows a zoomed version of panel A with standard logarithmic scaling to reduce visual artifacts. It should be noted that many cluster models do not appear to asymptote to the expected  $a_0$  value at low potential and substantial scatter is observed in the best fit curve.

behavior of the function suggests a serious flaw in the EMOND formalism.

Despite the defects discussed above, the correlation noted in HZ17 is observed; namely that the necessary  $A_0(\Phi)$  increases with increasing  $\Phi$ . As such, we followed their reasoning in fitting a simple model of  $A_0(\Phi)$  to the data. In an effort to minimize numerical difficulties, and because of the significant scatter of computed  $A_0(\Phi)$ , a simple exponential model was selected in the form

$$A_0(\Phi) = a_0 \exp((\Phi - \varphi)/\Phi_0). \quad (31)$$

A similar model was used in HZ17; however, we have introduced the parameter  $\varphi$  so as to recover the asymptotic behavior  $A_0(\Phi) \approx a_0$  as  $\Phi \rightarrow \varphi$ . Because of the exponential growth of  $A_0(\Phi)$ , systems with high accelerations and high potentials (neutron stars, black holes, etc.) would potentially be influenced by MOND effects, counter to observation. HZ17 proposed a more physically reasonable option which captures the same behavior as this model in low acceleration regimes. As our purpose here is only in regard to low acceleration systems, we adopt our simple model as sufficiently accurate in the regime of application. Best fit values for  $\varphi$  and  $\Phi_0$  were obtained from our cluster model via standard least-squares, yielding values of  $\varphi = -2.7 \text{ kpc}^2 \text{ Myr}^{-2}$  and  $\Phi_0 = 1.5 \text{ kpc}^2 \text{ Myr}^{-2}$ . The resulting curve is indicated in Figure 5.

Despite being a reasonably good fit to the clusters, considerable scatter is still observed in the model  $A_0(\Phi)$  function. As such, cluster models in the sample were regenerated; this time in the context of the best fit, fixed  $A_0(\Phi)$ . It is generally possible to do this in two ways: one may either require that the original  $\rho_g$  and  $T_g$  remain the same or one may require that the dynamical mass be limited to that of the gas. In the first case, EMOND will (in general scenarios) require the addition of a “phantom” mass component. The second case avoids requiring this additional component, but at the cost of changing the temperature.

In this work, we present only the later approach as it is more in line with the MOND paradigm. The resulting temperature profiles are provided in Figure 6. It is immediately clear that even for clusters with relatively tight fits to our model  $A_0(\Phi)$  curve, the subsequent change in the temperature profile becomes quite significant. In all of the cases in our sample, such a deviation would be very apparent in observations.

#### 4.1. Monte Carlo Constraints

In the previous section, it was established that EMOND fails to reproduce correct temperature profiles when applied to our cluster sample. In an effort to generalize these findings to a more comprehensive set of galaxy clusters, displaying a greater variation in their parameters and a closer link to the known cosmological constraints on galaxy clusters, a set of  $N = 500$  idealized clusters were generated in Newtonian gravity using the following prescription. Galaxy clusters were generated on the basis of two parameters,  $M_{500}$  and the gas fraction  $f_g$ . For each cluster, these parameters ( $M_{500}$  and  $f_g$ ) were generated between parameter values of  $10^{13} - 10^{15.5} M_\odot$  (log-uniformly distributed) and  $0.08 - 0.15$  (uniformly distributed), respectively. From  $M_{500}$ ,  $M_{200}$  was calculated approximately as  $M_{200} \approx 1.23 M_{500}$  and the corresponding NFW concentration parameter was calculated using the model of Diemer & Joyce (2019). Each cluster was assumed to be at redshift  $z = 0.05$ . The total mass of the system was then modeled as a TNFW profile as described in Baltz et al. (2009). A corresponding ICM component was generated from density profiles of the form of equation 15 with parameters determined by the TNFW profile parameters. This prescription sets the core radius to  $r_c = (1/2)r_{2500}$  and the scale radius to  $r_s = 1.1 \cdot r_{200}$ . The shape parameters  $\alpha$  and  $\beta$  were uniformly sampled on domains  $[0.1, 3]$  and  $[0.3, 0.8]$  respectively while  $\epsilon = 3$  in all clusters. The profile was then rescaled to produce the correct gas fraction as specified by the initial parameters. In

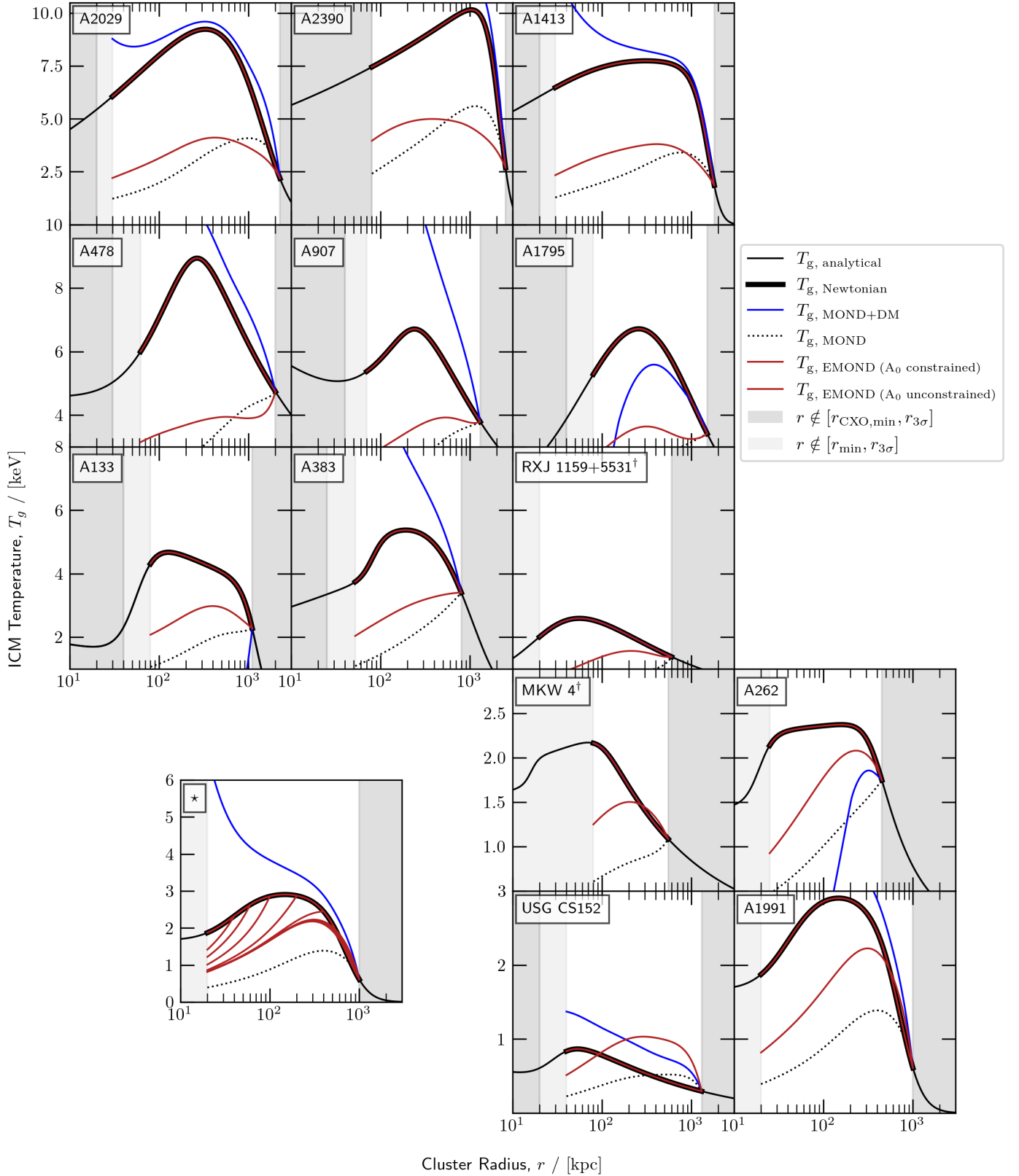


**Fig. 6.** Same as Figure 4 but including the EMOND paradigm. In the unconstrained case,  $A_0(\Phi)$  was adopted as necessary to reproduce the observables (see Figure 5). In the constrained case,  $A_0(\Phi)$  was fixed to equation 31 with parameters providing the best fit for the observed  $A_0(\Phi)$ . In all cases  $r_0 = r_{3\sigma}$  for each cluster and  $T_0 = T_{g,\text{analytical}}(r_0)$ . Shaded regions indicate radii outside of the observed domain  $[r_{\text{CXO,min}}, r_{3\sigma}]$  (dark grey) and radii outside of the physical region  $[r_{\text{min}}, r_{3\sigma}]$  (light grey).  $^\dagger$ MOND+DM Temperature profiles are self-consistent because  $r_{\text{viable}} \geq r_{3\sigma}$  for the indicated cluster; however, EMOND profiles need not be similarly behaved. Panel  $\star$  again indicates various choices of the temperature boundary condition for A1991.

this fashion, a fairly complete picture of galaxy clusters, as they are observed to appear in both simulation and observation, was generated. It should be remembered that the necessary  $A_0(\Phi)$  curve for which a system would be able to rid itself of the need for dark matter in an EMOND paradigm may be calculated explicitly from the corresponding Newtonian model. Thus, the aim of this undertaking is to take a comprehensive sample of semi-realistic cluster models and test them against EMOND.

To that end, the correct  $A_0$  curves were computed for each of the clusters in the sample. For each of the cluster models, the best fit  $A_0(\Phi)$  curve (as found above) was used to regenerate the cluster with the same baryonic profile but without dark matter and the resulting temperature profiles were computed to maintain hydrostatic equilibrium despite  $A_0(\Phi)$  not necessarily being the ideal curve for which the temperature would be invariant. Figure 7 shows the sample of clusters used in this analysis, their temperature profiles,  $A_0(\Phi)$  curves, and the resulting comparison between their EMOND and Newtonian temperatures. Notably, the observed error is consistent with those observed in the models based on Section 2.2, in some cases being as large as a factor of 3 different.

## 5. Discussion

In each of the paradigms described in this work, EMOND and MOND+DM, significant novel constraints were produced. These constraints prove to be a challenging hurdle for either formalism to contend with; especially given the already *ad hoc* nature of each of the extensions. Nonetheless, it would be premature to claim absolute rebuke of either theory. The underlying physics of galaxy clusters, particularly the assumption of (thermal) hydrostatic equilibrium and spherical symmetry, may affect observational inferences. These biases are expected (or needed) at the 10–40% level, which is generally smaller than the effects shown in this work, are therefore justify some confidence in our results. Nonetheless, the theoretical complexities of these biases have not been well constrained. Because these assumptions are so deeply embedded in the methodology presented, the value of the constraints produced may only come to their full value after a better understanding has been established of the underlying physics. Despite these clear limitations, the constraints here presented set a clear bar for the continued development of MONDian extensions intended to resolve MOND’s flaws at galaxy cluster scales. In the remainder of this section, we strive to discuss, in as critical and complete a sense possible, the implications of each of our findings for  $\Lambda$ CDM, for MOND, and for cluster physics in a general sense.

### 5.1. Fundamental Assumptions

In all of the theoretical work presented, two assumptions are presumed axiomatically: that clusters are spherically symmetric and that the intracluster medium maintains hydrostatic equilibrium throughout the system. Both of these assumptions are known to be flawed, to some degree, in all observed clusters. Regardless, both of these assumptions remain foundational to the derivation of galaxy cluster mass profiles, typically obtained from X-ray data (e.g., Vikhlinin et al. 2006; Eckert et al. 2019). Our understanding of hydrostatic equilibrium in galaxy clusters continues to be at the forefront of scientific progress in the field. Studies combining X-ray observations with secondary methods (e.g., weak lensing and SZ in Smith et al. 2016; Ghirardini et al. 2018, respectively) have shown hydrostatic mass biases ranging from 5–40%, indicating that many realistic systems have meaningful

non-thermal pressure components. In the work presented here, all such effects are ignored for the sake of mathematical viability and the generality of our approach; however, future work should broach the issue of non-thermal support in the context of MONDian galaxy clusters. As it concerns observation, the issue of non-thermal pressure support (while of great interest) is generally excused on the basis that such tensions are of the same order as assorted projection effects, calibration error, and other general sources of noise (Applegate et al. 2016). Due to these various effects and the implicit effects of our assumption of absolute hydrostatic equilibrium, it remains the case that any argument claiming to refute a MONDian perspective must produce scatter from expectation on the order of 40% to be valid without further examination.

Spherical symmetry also plays a key role in our analysis in this work; however, these effects are of somewhat lesser importance than those of hydrostatic equilibrium (Svensmark et al. 2015; Battaglia et al. 2012; Lebeau et al. 2023; Sarkar et al. 2022). It should be noted that various aspects of MONDian dynamics differ in the context of a non-spherical system. In particular, the equivalence between QUMOND and AQUAL, is only valid in a spherically symmetric system; which would then imply that further analysis should be done to determine if important variations arise when considering each of these flavours in the context of this work.

### 5.2. MOND+DM

The constraints presented in this work regarding MOND+DM extensions of MOND provide a serious test for such theories. Despite the various assumptions discussed in the previous section, the theoretical implications of Section 3 are nonetheless difficult to overlook. In the sample of clusters taken from Vikhlinin et al. (2006), the observation that many clusters contain maximal viable radii well within  $r_{200}$  suggests that even with the various biases and systematics of observation, such discrepancies should be observable in, at least, a subset of known systems. Furthermore, the observation that temperature profiles (in the context of HSE) should have different asymptotic behaviours to those of  $\Lambda$ CDM is a fundamental aspect of MONDian gravity. In fact, to alter the theory in such a way as to eliminate this issue, one would need to also eliminate the characteristic  $1/r$  behavior of the gravitational field in low acceleration regimes. Doing so would have severe consequences for MOND in those regimes where it currently succeeds. Thus, the findings of this work indicate that including additional phantom sources of mass in MONDian gravity theories is likely not a viable approach for the continued evolution of the MONDian research paradigm. As it stands, only a significant shift in our understanding of cluster physics, in turn massively altering the observations and assumptions underlying our analysis, would be sufficient to allow these extensions to have any chance at viability. From the standpoint of  $\Lambda$ CDM, it seems reasonable to conclude that MOND, in this particular manifestation, is completely and irreparably flawed in the cluster regime; a conclusion which places yet more pressure on the MONDian paradigm to confront these flaws if indeed it has any hope of challenging concordance cosmology. In the context of the MOND paradigm, the developments presented here may be seen as a step forward in our understanding of MOND’s behavior in galaxy clusters. Further work attempting to resolve the theoretical pitfalls that plague the paradigm in this regime can, with relative certainty, ignore the option of including additional, unobserved, mass. Doing so is also in better accord with developments in relativistic MOND and other modified gravity

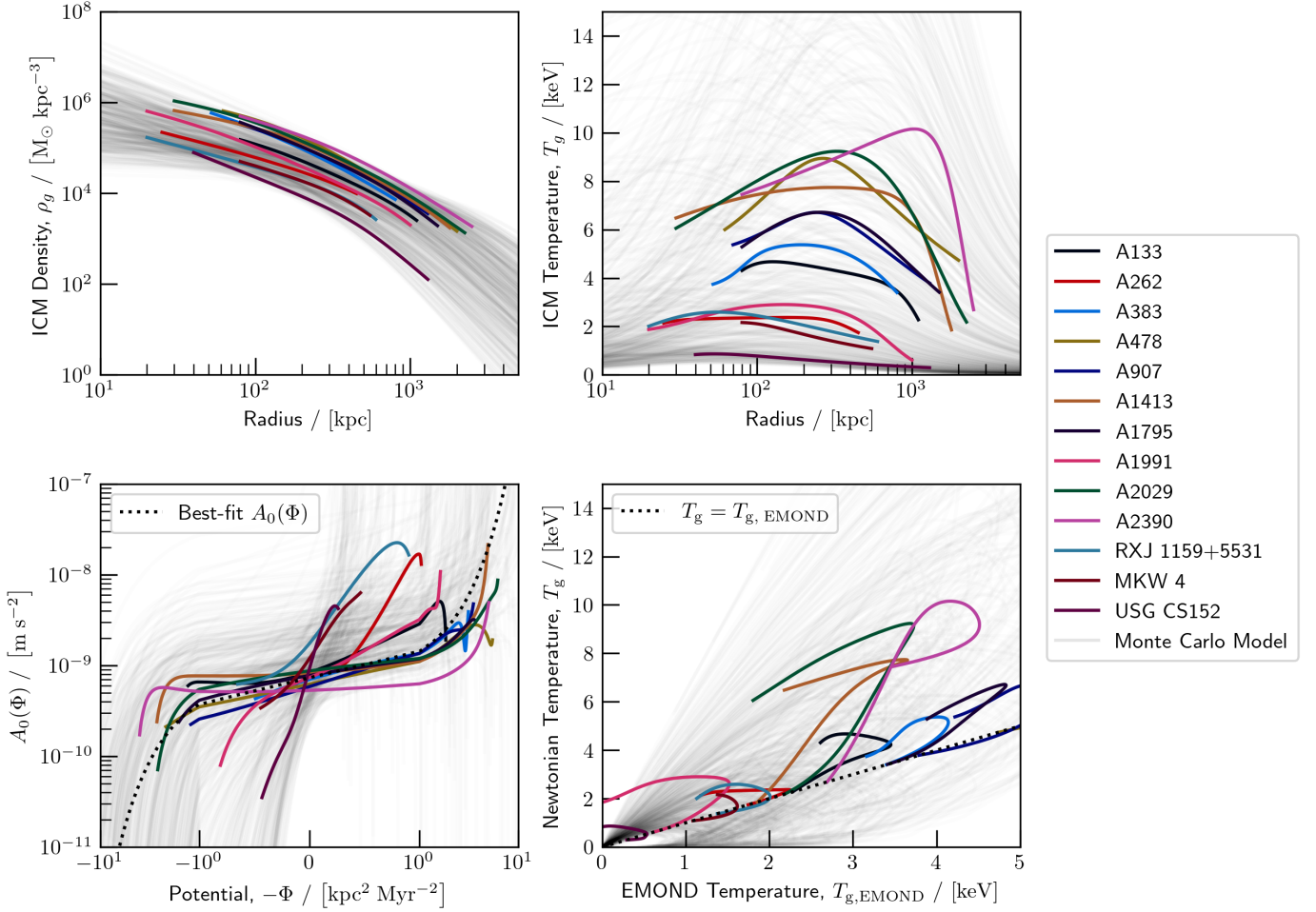


**Fig. 7.** EMOND analysis of the idealized cluster models of section 4.1. (*upper left*) Baryonic density profiles of each cluster in the Monte Carlo sample and those of the clusters in our observational sample. (*upper right*) ICM temperature profiles for each of the clusters. (*lower left*) Calculated (ideal)  $A_0(\Phi)$  curves for each of the simulated clusters as well as each of the clusters in the observational sample. The best fit curve determined in section 4 is also plotted and provides a good fit. (*lower right*) The  $(T_g, T_{g, \text{EMOND}})$  curve followed by each cluster in the MC sample and the observational sample. The dotted line indicates the  $T_g = T_{g, \text{EMOND}}$  followed by a cluster for which the ideal  $A_0(\Phi)$  curve corresponds to the best-fit model. In general, MC clusters diverge from  $T_g = T_{g, \text{EMOND}}$  given any perturbation in  $A_0$ , leading to the "leaf-like"  $(T_g, T_{g, \text{EMOND}})$  curves. It should be noted that *some* MC clusters do lie nearly perfectly along the ideal line.

theories and effectively eliminates a significant number of dead ends.

### 5.3. EMOND

Whereas the implications regarding MOND+DM were straightforward, EMOND presents a more complex picture. There are clear flaws in the formalism, particularly in regard to the gauge dependence of the  $A_0(\Phi)$  function; however, such flaws may show themselves to be merely the effect of relying on an empirical theory. In our analysis, the choice to make  $A_0(\Phi)$  a function of  $\Phi - \varphi$  effectively eliminates the issue of gauge dependence so long as the (supposed) fundamental theory leading to EMOND provides some context under which  $\Phi - \varphi$  is resolved in a gauge invariant way. Zhao & Famaey (2012) observed in their original work that this may arise from the weak field approximation of a more consistent, relativistic, form of the underlying theory.

If one accepts that the inelegant aspects of the formalism may be disregarded, then the implications of our analysis still cast doubt on EMOND's capacity to account for the missing mass problem in clusters of galaxies. In applying HSE to the cluster sample of Vikhlinin et al. (2006), it is clear that the best-fit  $A_0(\Phi)$

allows too much scatter against each cluster's ideal  $A_0(\Phi)$  and is manifestly incompatible with observations of the clusters.

In each of the 13 clusters included, deviations in the temperature profiles calculated by enforcing a uniform  $A_0(\Phi)$  are well within the range for which they would be apparent in X-ray observations. Thus, the fact that such discrepancies are not observed implies that EMOND warrants serious doubt as a potential approach for correcting MOND in clusters of galaxies.

On the other hand, when analyzed in the context of the cosmologically motivated cluster models in Section 4.1, EMOND fares somewhat better on a cluster-by-cluster basis. While the Monte-Carlo results support the scatter determined in each of the observed clusters, they also suggest that, depending on choice of "best"  $A_0$  and permitted bias, a large swath of the parameter space may be well described by EMOND. Regardless, it is our assessment that the deviations observed in the temperature profiles of the observationally produced models present a serious constraint to EMOND theory. More work should be done to establish whether or not the deviations predicted here can be evaded by more accurate observational methodology. Independent of one's preference regarding which models are most valid,



this work firmly establishes an observational context through which to test the extended MOND paradigm.

## 6. Conclusions

In this work, we have explored the current position of the MOND research paradigm in galaxy clusters and illustrated many of the persistent difficulties involved in generating an observationally consistent MOND theory. By analyzing a set of galaxy clusters using the assumption of hydrostatic equilibrium, we demonstrated that there were severe weaknesses in both the MOND+DM paradigm and the EMOND paradigm. In the case of MOND+DM, we demonstrate that there exist strong constraints on the physicality of the necessary dark matter component, which bring into question the validity of the theory at large radii. Nonetheless, our analysis of the MOND+DM paradigm was not conclusively at odds with observation. Our constraints, when applied to ideal models of galaxy clusters, paint a worrying picture with many of the clusters failing to be consistent with the MOND approach well within the expected observable domain.

In our analysis of the Extended MOND approach, we demonstrated that, while our cluster sample was well fit by reasonable functions for  $A_0(\Phi)$ , the resulting scatter in that relation was far too significant to accurately reproduce galaxy clusters' temperature profiles. A secondary analysis of a broader, but more theoretical, set of cluster models indicated similar scatter; however, some systems were sufficiently close to the ideal  $A_0(\Phi)$  that EMOND reproduced to correct temperature profiles. Nonetheless, as an ensemble, deviations as large as a factor of 3 in the temperature profiles are predicted and should be observable in, at least, a subset of systems. We therefore conclude that the EMOND theory appears to be at odds with observed galaxy clusters, despite its initial success in describing the dynamical mass of such systems. Further work is necessary to more thoroughly constrain the extent to which biases may soften the findings of this work; however, we find it implausible that any bias (or combination thereof) could be sufficiently large to permit the observed scatter in the EMOND temperatures.

**Acknowledgements.** This work was made possible with data from the *Chandra* X-ray Observatory and was initially analyzed by Vikhlinin et al. (2006). Idealized models of galaxy clusters were made possible with the `cluster_generator` package written by John ZuHone and Eliza Diggins. The package may be obtained at [https://www.github.com/jzuhone/cluster\\_generator](https://www.github.com/jzuhone/cluster_generator). Visualizations were made possible using Matplotlib (Hunter 2007), particularly the colormaps provided in the `cmocean` package (Thyng et al. 2016).

## References

Aalseth, C. E., Barbeau, P., Bowden, N., et al. 2011a, *Physical Review Letters*, 106, 131301  
Aalseth, C. E., Barbeau, P., Colaresi, J., et al. 2011b, *Physical Review Letters*, 107, 141301  
Aguirre, A., Schaye, J., & Quataert, E. 2001, *The Astrophysical Journal*, 561, 550  
Angloher, G., Bento, A., Bucci, C., et al. 2014, *The European Physical Journal C*, 74, 1  
Angus, G. W. 2009, *Monthly Notices of the Royal Astronomical Society*, 394, 527  
Angus, G. W., Diaferio, A., Famaey, B., & van der Heyden, K. J. 2013, *Monthly Notices of the Royal Astronomical Society*, 436, 202  
Applegate, D. E., Mantz, A., Allen, S. W., et al. 2016, *MNRAS*, 457, 1522  
Baltz, E. A., Marshall, P., & Oguri, M. 2009, *Journal of Cosmology and Astroparticle Physics*, 2009, 015  
Battaglia, N., Bond, J. R., Pfrommer, C., & Sievers, J. L. 2012, *ApJ*, 758, 74  
Begeman, K., Broeils, A., & Sanders, R. 1991, *Monthly Notices of the Royal Astronomical Society*, 249, 523

Bekenstein, J. & Milgrom, M. 1984, *Astrophysical Journal*, Part 1 (ISSN 0004-637X), vol. 286, Nov. 1, 1984, p. 7-14. Research supported by the MINERVA Foundation., 286, 7  
Bekenstein, J. D. 2004, *Physical Review D*, 70, 083509  
Berezhiani, L. & Khoury, J. 2015, *Physical Review D*, 92, 103510  
Berteaud, J., Francesca, C., Iguaz, J., Serpico, P. D., & Siebert, T. 2023, in *EPJ Web of Conferences*, Vol. 280, EDP Sciences, 07003  
Biffi, V., Borgani, S., Murante, G., et al. 2016, *The Astrophysical Journal*, 827, 112  
Brunetti, G. & Jones, T. W. 2014, *International Journal of Modern Physics D*, 23, 1430007  
Buote, D. A. & Humphrey, P. J. 2012a, *Monthly Notices of the Royal Astronomical Society*, 421, 1399  
Buote, D. A. & Humphrey, P. J. 2012b, *Monthly Notices of the Royal Astronomical Society*, 421, 1399  
Carr, B., Kohri, K., Sendouda, Y., & Yokoyama, J. 2010, *Physical Review D*, 81, 104019  
Carr, B. & Kühnel, F. 2020, *Annual Review of Nuclear and Particle Science*, 70, 355  
Cavaliere, A. & Fusco-Femiano, R. 1976, *Astronomy and Astrophysics*, vol. 49, no. 1, May 1976, p. 137-144., 49, 137  
Diemer, B. & Joyce, M. 2019, *ApJ*, 871, 168  
Eckert, D., Ettori, S., Pointecouteau, E., van der Burg, R., & Loubser, S. 2022, *Astronomy & Astrophysics*, 662, A123  
Eckert, D., Ghirardini, V., Ettori, S., et al. 2019, *A&A*, 621, A40  
Ensslin, T. A., Biermann, P. L., Kronberg, P. P., & Wu, X.-P. 1997, *The Astrophysical Journal*, 477, 560  
Felten, J. E. 1984, *Astrophysical Journal*, Part 1 (ISSN 0004-637X), vol. 286, Nov. 1, 1984, p. 3-6., 286, 3  
Fukugita, M., Hogan, C., & Peebles, P. 1998, *The Astrophysical Journal*, 503, 518  
Gerbal, D., Durret, F., Lachieze-Rey, M., & Lima-Neto, G. 1992, *Astronomy and Astrophysics*, 262, 395  
Ghirardini, V., Ettori, S., Eckert, D., et al. 2018, *A&A*, 614, A7  
Hodson, A. O. & Zhao, H. 2017, *Astronomy & Astrophysics*, 598, A127  
Hodson, A. O., Zhao, H., Khoury, J., & Famaey, B. 2017, *Astronomy & Astrophysics*, 607, A108  
Hunter, J. D. 2007, *Computing in Science & Engineering*, 9, 90  
Kent, S. M. 1987, *The Astronomical Journal*, 93, 816  
Labbé, I., van Dokkum, P., Nelson, E., et al. 2023, *Nature*, 1  
Landau, L. D. 2013, *The classical theory of fields*, Vol. 2 (Elsevier)  
Lasserre, T. & Collaboration, E. 2000, *arXiv preprint astro-ph/0002253*  
Lau, E. T., Kravtsov, A. V., & Nagai, D. 2009, *The Astrophysical Journal*, 705, 1129  
Lebeau, T., Sorce, J. G., Aghanim, N., Hernández-Martínez, E., & Dolag, K. 2023, *arXiv e-prints*, arXiv:2310.02326  
Lelli, F., McGaugh, S. S., & Schombert, J. M. 2016, *The Astrophysical Journal Letters*, 816, L14  
McGaugh, S. S. 2012, *The Astronomical Journal*, 143, 40  
Merritt, D. 2020, *A philosophical approach to MOND: Assessing the Milgromian research program in cosmology* (Cambridge University Press)  
Milgrom, M. 1983a, *Astrophysical Journal*, Part 1 (ISSN 0004-637X), vol. 270, July 15, 1983, p. 365-370. Research supported by the US-Israel Binational Science Foundation., 270, 365  
Milgrom, M. 1983b, *The Astrophysical Journal*, 270, 371  
Milgrom, M. 2008, *New Astronomy Reviews*, 51, 906  
Milgrom, M. 2009, *Physical Review D*, 80, 123536  
Milgrom, M. 2010, *Monthly Notices of the Royal Astronomical Society*, 403, 886  
Nelson, K., Lau, E. T., & Nagai, D. 2014, *The Astrophysical Journal*, 792, 25  
Nelson, K., Rudd, D. H., Shaw, L., & Nagai, D. 2012, *The Astrophysical Journal*, 751, 121  
Pearce, F. A., Kay, S. T., Barnes, D. J., Bower, R. G., & Schaller, M. 2020, *Monthly Notices of the Royal Astronomical Society*, 491, 1622  
Perivolaropoulos, L. & Skara, F. 2022, *New Astronomy Reviews*, 101659  
Planck Collaboration, Aghanim, N., Akrami, Y., et al. 2020, *A&A*, 641, A6  
Pointecouteau, E. & Silk, J. 2005, *Monthly Notices of the Royal Astronomical Society*, 364, 654  
Rosner, R. & Tucker, W. 1989, *The Astrophysical Journal*, 338, 761  
Rubin, V. C. & Ford Jr, W. K. 1970, *The Astrophysical Journal*, 159, 379  
Ryden, B. 2017, *Introduction to cosmology* (Cambridge University Press)  
Sarazin, C. L. 1986, *Reviews of Modern Physics*, 58, 1  
Sarkar, K. C., Dey, A., & Sharma, P. 2022, *MNRAS*, 516, 992  
Savchenko, V., Ferrigno, C., Kuulkers, E., et al. 2017, *The Astrophysical Journal Letters*, 848, L15  
Schneider, P. 2006, *Extragalactic astronomy and cosmology: an introduction*, Vol. 146 (Springer)  
Shi, X. & Komatsu, E. 2014, *MNRAS*, 442, 521  
Skordis, C. & Zlosnik, T. 2012, *Physical Review D*, 85, 044044  
Skordis, C. & Zlosnik, T. 2019, *Physical Review D*, 100, 104013



- Smith, G. P., Mazzotta, P., Okabe, N., et al. 2016, MNRAS, 456, L74
- Svensmark, J., Wojtak, R., & Hansen, S. H. 2015, MNRAS, 448, 1644
- Thyng, K. M., Greene, C. A., Hetland, R. D., Zimmerle, H. M., & DiMarco, S. F. 2016, Oceanography, 29
- Tisserand, P., Le Guillou, L., Afonso, C., et al. 2007, Astronomy & Astrophysics, 469, 387
- Vazza, F., Angelinelli, M., Jones, T., et al. 2018, Monthly Notices of the Royal Astronomical Society: Letters, 481, L120
- Verheijen, M. A. 2001, The Astrophysical Journal, 563, 694
- Vikhlinin, A., Kravtsov, A., Forman, W., et al. 2006, The Astrophysical Journal, 640, 691
- White, S. D., Frenk, C. S., & Davis, M. 1983, Astrophysical Journal, Part 2- Letters to the Editor (ISSN 0004-637X), vol. 274, Nov. 1, 1983, p. L1-L5., 274, L1
- Zhao, H. & Famaey, B. 2012, Physical Review D, 86, 067301
- Zwicky, F. 1937, The Astrophysical Journal, 86, 217

## Appendix A: Derivation of Equation 24 and Related Results

In order to produce a physically allowable phantom mass profile,  $\rho_{\text{ph}} \geq 0$ , or (equivalently),  $\partial_r M_{\text{ph}} \geq 0$ . Let

$$\gamma(r) = \frac{G\tilde{M}_{\text{dyn}}(< r)}{a_0 r^2} = \left| \frac{\mathbf{a}(r)}{a_0} \right|. \quad (\text{A.1})$$

This should be interpreted as the *relative acceleration scale* for the cluster at radius  $r$ , with  $\gamma \ll 1$  implying a deep-MOND regime and  $\gamma \gg 1$  implying a Newtonian regime. By differentiating Equation 18;

$$\partial_r M_{\text{ph}}(< r) = \partial_r \left[ \tilde{M}_{\text{dyn}}(< r) \mu \left( \frac{|\nabla \Phi|}{a_0} \right) \right] - \partial_r M_g(< r). \quad (\text{A.2})$$

Recall that  $\nabla \Phi$  is *invariant* between each of the two paradigms in the context of the theorem, *ergo*,

$$\frac{|\nabla \tilde{\Phi}|}{a_0} = \frac{|\nabla \Phi|}{a_0} = \gamma(r). \quad (\text{A.3})$$

As such, the inequality of interest may be written in the form

$$\partial_r \tilde{M}_{\text{dyn}}(< r) \left\{ \mu(\gamma) + \gamma \partial_\gamma \mu(\gamma) \right\} - \frac{2\gamma}{r} \tilde{M}_{\text{dyn}}(< r) \partial_\gamma \mu(\gamma) \geq \partial_r M_g(< r). \quad (\text{A.4})$$

Further simplification here is not particularly fortuitous; however, if one constrains the class of interpolation functions  $\mu$  to the form

$$\mu_\alpha(x) = \frac{x}{(1 + x^\alpha)^{1/\alpha}}, \quad (\text{A.5})$$

then

$$\partial_\gamma \mu(\gamma) = \frac{\mu(\gamma)}{\gamma(\gamma^\alpha + 1)}, \quad (\text{A.6})$$

which implies that

$$\mu_\alpha(\gamma) \left\{ \partial_r \tilde{M}_{\text{dyn}}(< r) + \frac{r \partial_r \tilde{M}_{\text{dyn}}(< r) - 2\tilde{M}_{\text{dyn}}(< r)}{r(\gamma^\alpha + 1)} \right\} \geq \partial_r M_g(< r) \geq 0 \quad (\text{A.7})$$

with the final inequality following on physical assumptions about the gas profile. Further simplification results in

$$\frac{d \ln(\tilde{M}_{\text{dyn}}(< r))}{dr} \geq \frac{2}{r(\gamma^\alpha + 2)} = \frac{1}{r \left( \frac{\gamma^\alpha}{2} + 1 \right)} \geq \frac{1}{r(\gamma^\alpha + 1)}. \quad (\text{A.8})$$

This is the extent of the analysis without further simplification. Because  $\gamma$  has no upper bound, there is no further relaxation without imposing cases.

1. ( $\gamma > 1$ ): In this case, the cluster resides in a Newtonian regime and because  $\gamma > 1$ ,

$$\forall r, \exists \alpha \text{ s.t. } \frac{d \ln(\tilde{M}_{\text{dyn}}(< r))}{dr} \geq \frac{1}{r(\gamma^\alpha + 1)}. \quad (\text{A.9})$$

This value of  $\alpha$ , denoted  $\bar{\alpha}$ , may be thought of as the minimal interpolation scale at which the cluster is viable to a radius  $r$ .

2. ( $\gamma \leq 1$ ): In this case, we note that  $\gamma \geq \gamma^\alpha$  for any positive integer  $\alpha$ ; therefore the inequality simplifies to the form

$$\frac{d \ln(\tilde{M}_{\text{dyn}}(< r))}{dr} \geq \frac{1}{r(\gamma + 1)} \geq \frac{1}{2r}. \quad (\text{A.10})$$

Written in terms of the density,

$$\tilde{\rho}_{\text{dyn}}(r) \geq \frac{\tilde{M}_{\text{dyn}}(< r)}{8\pi r^3} \geq \frac{\langle \tilde{\rho}_{\text{dyn}} \rangle_r}{6}; \quad (\text{A.11})$$

where  $\langle \tilde{\rho}_{\text{dyn}} \rangle_r$  denotes the average density of the cluster within the radius  $r$ .